

# Unsupervised Learning of High-resolution Light Field Imaging via Beam Splitter-based Hybrid Lenses

Jianxin Lei<sup>1</sup>, Chengcai Xu<sup>1</sup>, Langqing Shi<sup>1</sup>, Junhui Hou<sup>2</sup>✉, Ping Zhou<sup>1</sup>✉

<sup>1</sup>Southeast University <sup>2</sup>City University of Hong Kong

{leijsx, zhouping}@seu.edu.cn, jh.hou@cityu.edu.hk

## Abstract

In this paper, we design a beam splitter-based hybrid light field imaging prototype to record 4D light field image and high-resolution 2D image simultaneously, and make a hybrid light field dataset. The 2D image could be considered as the high-resolution ground truth corresponding to the low-resolution central sub-aperture image of 4D light field image. Subsequently, we propose an unsupervised learning-based super-resolution framework with the hybrid light field dataset, which adaptively settles the light field spatial super-resolution problem with a complex degradation model. Specifically, we design two loss functions based on pre-trained models that enable the super-resolution network to learn the detailed features and light field parallax structure with only one ground truth. Extensive experiments demonstrate the same superiority of our approach with supervised learning-based state-of-the-art ones. To our knowledge, it is the first end-to-end unsupervised learning-based spatial super-resolution approach in light field imaging research, whose input is available from our beam splitter-based hybrid light field system. The hardware and software together may help promote the application of light field super-resolution to a great extent.

## 1. Introduction

Light field (LF) imaging has gained widespread attention due to its convenience and accuracy in recording and reconstructing 3-dimensional (3D) scenes [45]. The 4D information (2D spatial and 2D angular) recorded by LF imaging technology can help realize various applications, such as digital refocusing [11, 34], 3D reconstruction [6, 19, 45], virtual reality [39], etc. The emergence of the commercial LF camera, i.e. Lytro Illum [1] and Rytrix [2], promote the development of LF imaging. However, due to the limitation of the bandwidth product of spatial-angular resolution [35], the spatial resolution of LF cameras is usually significantly lower than that of digital single-lens re-

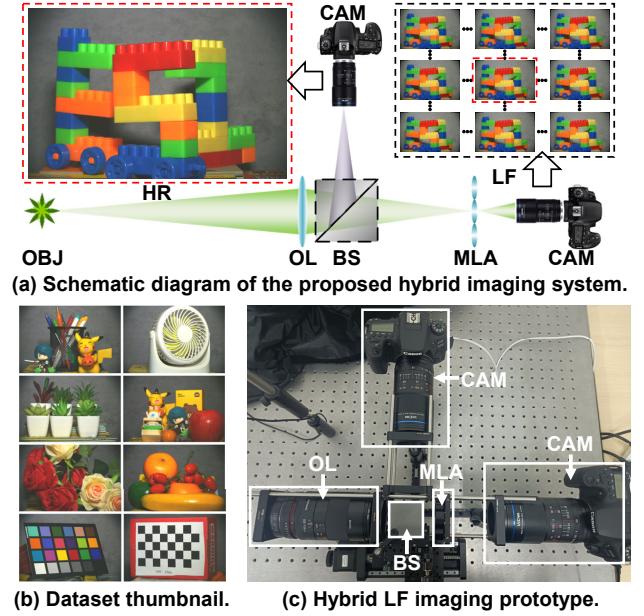


Figure 1. The beam splitter-based hybrid LF imaging prototype. OBJ: object, OL: objective lens, BS: beam splitter, MLA: micro-lens array, CAM: camera, HR: 2D HR image, LF: 4D LF image.

flex (DLSR) cameras, which restricts the further promotion of LF cameras. Improving the spatial resolution through advanced hardware is an accessible approach with higher-density sensors, but it would greatly increase the economic cost of the system, unfortunately.

Recently, many methods for LF spatial super-resolution (SR) have been proposed. Most of them are external-supervised learning-based (ESLB) methods, which use one-to-one ground truth as strong supervision to guide network training. In general, the performance of the ESLB SR methods [7, 9, 15, 16, 18, 23, 24, 32, 33, 37, 38, 40, 42] is better, when compared with non-learning-based (NLB) methods [5, 31] and self-supervised learning-based (SSLB) methods [10, 26]. However, it is complicated for an LF system to obtain enough ground truth in real-world appli-

cations, and there is a large domain shift between real-world LF data and simulated LF data. These ESLB methods inevitably face the domain shift problem and they cannot super-resolve real-world data as they do with the simulated data.

To address these issues above, we design a beam splitter-based hybrid LF imaging prototype first, as shown in Fig. 1, which records two types of images simultaneously: a 4D LF image with low spatial resolution sub-aperture images (SAIs) and a high spatial resolution 2D image. It is worth noting that the 2D image is consistent in view with the central SAI of the 4D LF image, and a dataset comprising images recorded by the hybrid LF imaging prototype is made for our spatial SR network.

Accordingly, we propose an LF spatial SR network that uses data recorded by our hybrid LF system as input. It is an unsupervised learning-based (USLB) network because the side views of 4D LF to be super-resolved do not have ground truth. Extensive experiment results show our USLB LF spatial SR method has similar or even better performance compared with the state-of-the-art (SoTA) LF image SR methods [5, 7, 10, 18, 24, 31, 33, 37] on public datasets. Moreover, with the reasonable application of our own method, the obtained SR results on our hybrid LF dataset exhibit superb visual performance and maintain the LF structure well.

In summary, our primary contributions are as follows:

- To overcome the limitation of the resolution bandwidth product of LF cameras, we design a beam splitter-based hybrid LF imaging prototype and make a dataset with 2D and 4D hybrid images.
- We propose a USLB LF spatial SR network, whose input is from our hybrid system. To achieve unsupervised learning and extract features sufficiently, we design two loss functions based on two pre-trained models to guide spatial SR learning.

## 2. Related Work

### 2.1. Light Field Image Spatial Super-resolution

LF image spatial SR aims at improving the spatial resolution for all SAIs simultaneously. With the development of deep learning methods, Yoon et al. [38] proposed the first CNN-based SR algorithm for LF images (LFCNN), which improved the spatial and angular resolution of LF images by processing SAIs independently through multiple SRCNN-based sub-networks. After that, several ESLB methods [15, 32, 33, 37, 40, 42] have been designed to improve the spatial resolution of LF images through different network architectures. Among them, Wang et al. [33] organized SAIs into macro-pixel image, and proposed a disentangling mechanism to fully explore the information of 4D LF. Recently, Liang et al. [23] applied Transformers to

LF image SR (termed LFT), and then proposed EPIT [24] to learn the non-local spatial-angular correlation for LF image SR. Although the current ESLB methods have achieved excellent SR performance, their application to real-world LF can be challenging due to the lack of sufficient ground truth and the domain shift between real-world test data and simulated training data. To address these issues, Cheng et al. [10] solved the domain gap problem in LF spatial SR via the zero-shot learning, Sheng et al. [26] designed an SSLB method for improving spatial and angular resolution of LF simultaneously.

### 2.2. Hybrid Light Field Imaging

According to the relationship between the optical axes of the LF and DSLR camera, there were mainly two kinds of hybrid LF imaging systems. The most common hybrid LF imaging system is equipped with a Lytro Illum LF camera and a DSLR camera, whose optical axes are parallel to each other [3, 5, 30, 36]. Based on this hybrid system, Boomnathan et al. [5] proposed a patch matching-based algorithm (named PaSR) to improve LF resolution by hybrid input. Zheng et al. [44] combined an exemplar-based approach and a learning-based approach for LF SR. Recently, to establish and utilize the relationship between the LR LF image and the 2D HR image, Chen et al. [9] designed an LF feature alignment module and a multi-level spatial-angular feature enhancement module. Despite the simple and accessible structure, there is still an inconsistency between LF images and HR images in this hybrid LF imaging system as their far viewpoints. The SR methods based on this kind of hybrid imaging system often suffer extreme challenges in SR performance, as there is no one-to-one relationship between the HR 2D image and one of the SAIs.

Different from the aforementioned hybrid LF system, Wang et al. [31] proposed an LF attachment prototype with hybrid lenses, they used a LF lens attachment that can convert a DSLR camera into a hybrid LF camera. However, there is a problem of low acquisition and color inconsistency across views. Based on this prototype, Wang et al. [31] improved the resolution of side-view SAIs by iterative refinement combining patch-based SR results with depth-based synthesis. Zhao et al. [43] designed HCSR, which transferred the details from the HR image to the LR side-view SAIs to obtain high-quality LF. Recently, Chang et al. [7] used layered refinement for designing the LF SR network, which has obvious advantages in cases of large disparity range. Jin et al. [16, 18] proposed a framework that achieved impressive SR performance with two complementary and parallel research lines, namely SR-Net and Warp-Net, and their advantages were combined via attention-guided fusion. Note that Jin et al. [18] used color perturbation to augment the training dataset to address the color inconsistency in the real-world hybrid dataset [31].

For LF SR with hybrid input, The super-resolved LF obtained by the NLB methods [5, 31, 44] have the drawbacks of blur and distortion. Although the ESLB methods [7, 9, 16, 18] can achieve excellent performance, they rely on sufficient ground truth.

### 3. Hybrid 4D LF Imaging Prototype

**Setup.** Our beam splitter-based hybrid LF imaging prototype is primarily equipped with an objective lens, a cubic beam splitter, a co-located low spatial resolution LF imaging subsystem, and a high spatial resolution traditional imaging subsystem. As shown in Fig. 1(a), the light emitted by the object point is received and concentrated by the objective lens. It is then divided into two parts (transmitted light and reflected light) by the beam splitting plane of the cubic beam splitter. The transmitted part is received by micro-lens array (MLA) and projected onto the CCD image sensor to record the 4D LF image with low spatial resolution 2D SAIs. Meanwhile, the reflected part is projected onto the traditional camera to record the high spatial resolution 2D traditional image.

As shown in Fig. 1(c), the prototype consists of the objective lens (focal length 100mm, F2.8), the cubic beam splitter (cube size 50mm, spectral ratio 30R/70T), an MLA (focal length 2mm, microlens pitch 0.063mm), two relay lens (focal length 100mm, F2.8) and two photosensors (Canon 90D). All these modules are mounted via kinematic mounts (Thorlabs) to allow fine adjustment with respect to the optical axis.

**Data Processing and Dataset.** We accomplish the joint calibration of the hybrid imaging system via the checkerboard, whose pattern is  $5 \times 8$  and grid size is  $12 \times 12$ mm. As shown in Fig. 1(b), some colorful books, boxes, toy blocks, flowers, fruits, and toys are used as samples for our hybrid LF dataset. The size of 2D HR image is  $6960 \times 4640$  pixels, the size of 2D SAI is  $329 \times 217$  pixels and the size of microlens image is  $19 \times 19$  pixels.

To ensure the color consistency between 2D HR images and LF images, we use the LSA method [4, 14] to calculate the transformation matrix for color correction by capturing the color chart model (Datacolor SpyderCheckr 24). To maintain the view consistency between the 2D HR image and the central SAI of LF, we compute the affine transformation matrix via feature points in two corresponding images, and then we crop and scale the 2D HR image that is the ground truth of the central SAI. Finally, the dataset contains 189 pairs of 2D HR images and 4D LR LF images.

### 4. Proposed Method

**Overview.** Let  $\mathcal{L}(\mathbf{u}, \mathbf{x}) \in \mathbb{R}^{M \times N \times W \times H}$  denote the 4D LF with  $M \times N \times W \times H$  resolution, where  $\mathbf{u} = \{(u, v) \mid 1 \leq u \leq M, 1 \leq v \leq N\}$  represents angular coordinates,  $\mathbf{x} = \{(x, y) \mid 1 \leq x \leq W, 1 \leq y \leq H\}$  represents spatial coordinates.

Let  $I_{\mathbf{u}_0}$  represent the central SAI with spatial resolution as  $W \times H$  and  $I_{\mathbf{u}_0}^h \in \mathbb{R}^{\alpha W \times \alpha H}$  denote the 2D HR image, where  $\mathbf{u}_0 = (u_0, v_0)$  is the angular coordinates of the central SAI, and  $\alpha$  is an up-sample scale factor. As shown in Fig. 2, our proposed USLB LF spatial SR framework can be divided into the first stage of pre-training the central view synthesis network (CVS-Net) and the backward degradation network (BD-Net), and the second stage of training the hybrid light field spatial super-resolution network (HLFSSR-Net).

**Pre-training stage.** As shown in Fig. 2(a), in the CVS-Net, 8 side-view SAIs denoted by  $\mathcal{L}_s$  are divided into two sets:  $\mathcal{L}_{s_1}$  and  $\mathcal{L}_{s_2}$ . Then,  $\mathcal{L}_{s_1}$  and  $\mathcal{L}_{s_2}$  are randomly selected as inputs. The CVS-Net is pre-trained to learn the mapping relationship between  $\mathcal{L}_s$  and  $I_{\mathbf{u}_0}$ , i.e.,

$$\tilde{I}_{\mathbf{u}_0} = f_{CVS}(\mathcal{L}_s). \quad (1)$$

As shown in Fig. 2(b), in the BD-Net,  $I_{\mathbf{u}_0}^h$  is used as input, and the BD-Net is pre-trained to learn the degradation process from  $I_{\mathbf{u}_0}^h$  to  $I_{\mathbf{u}_0}$ , i.e.,

$$\hat{I}_{\mathbf{u}_0} = f_{BD}(I_{\mathbf{u}_0}^h). \quad (2)$$

**Training stage.** As shown in Fig. 2(c), during the training stage,  $\mathcal{L}$  and  $I_{\mathbf{u}_0}^h$  are simultaneously fed into the HLFSSR-Net to learn the residual map from low spatial resolution  $\mathcal{L}$  to high spatial resolution  $\tilde{\mathcal{L}}^h \in \mathbb{R}^{M \times N \times \alpha W \times \alpha H}$ . The bicubic up-sample results of  $\mathcal{L}$  are added to the residual map to obtain the spatial super-resolved LF  $\tilde{\mathcal{L}}^h$ . The problem of reconstructing  $\tilde{\mathcal{L}}^h$  from the hybrid input can be implicitly formulated as:

$$\tilde{\mathcal{L}}^h = f_{HLFSSR}(\mathcal{L}, I_{\mathbf{u}_0}^h). \quad (3)$$

Then, the side-view SAIs  $\tilde{\mathcal{L}}_s^h$  in  $\tilde{\mathcal{L}}^h$  are divided into two sets and fed into the pre-trained CVS-Net through the same way as the first stage. The parameters of the pre-trained CVS-Net are frozen, and the output of the CVS-Net is the HR central SAI  $\tilde{I}_{\mathbf{u}_0}^h \in \mathbb{R}^{\alpha H \times \alpha W}$ , i.e.,

$$\tilde{I}_{\mathbf{u}_0}^h = f_{CVS}^*(\tilde{\mathcal{L}}_s^h), \quad (4)$$

where  $*$  indicates the frozen parameters.

$\tilde{\mathcal{L}}^h$  is fed into the BD-Net. The output of BD-Net is  $\tilde{\mathcal{L}}$ , which has the same scale with the input  $\mathcal{L}$ , i.e.,

$$\tilde{\mathcal{L}} = f_{BD}^*(\tilde{\mathcal{L}}^h). \quad (5)$$

#### 4.1. LF Central View Synthesis Network

As shown in Fig. 2(c), the CVS-Net synthesizes the central SAI from the side-view SAIs super-resolved by the HLFSSR-Net during forward propagation, then transmits

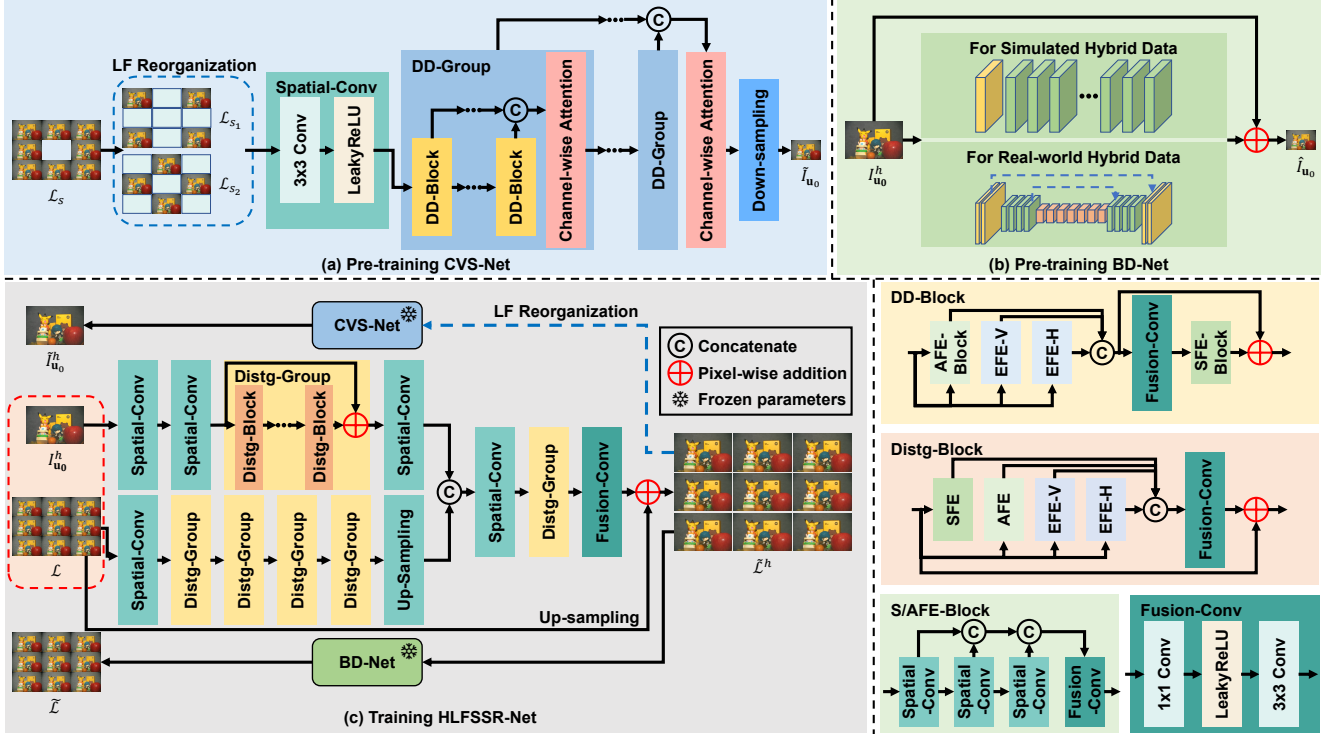


Figure 2. Illustration of the flowchart of our unsupervised learning-based high-resolution 4D LF reconstruction framework. A  $3 \times 3$  LF is used as an example for illustration. SFE, AFE, EFE-V, and EFE-H represent the spatial, angular, vertical EPI, and horizontal EPI feature extractor [33]. These four feature extractors can disentangle LFs into different subspaces.

the gradient from the loss function back to the HLFSSR-Net in backpropagation. To ensure that the HLFSSR-Net accurately learns the detailed features of the 2D HR image  $I_{u_0}^h$  with the assistance of the CVS-Net, we design some specific strategies which are outlined below.

**LF reorganization.** As the spatial information contained in all side-view SAIs is redundant for synthesizing the central SAI, it is essential to ensure uniform propagation of gradients from synthesized central SAI back to the input side-view SAIs during backpropagation, so that all side-view SAIs are treated with similar contributions in the synthesis. Therefore, as shown in Fig. 2(a), we reorganize all side-view SAIs into 2 groups of  $2 \times 2$  SAIs as the input of the CVS-Net.

**Deep disentangling mechanism.** Due to the difference in image scales processed by the CVS-Net in the first pre-training and second training stages, it is essential for the CVS-Net to maintain both scale and content invariance. Therefore, we introduce the deep disentangling (DD) mechanism [28] to the CVS-Net with a three-level structure. As shown in Fig. 2(a), the first level and the second level structure are constructed by the DD-Group and the DD-Block, respectively. The third level structure consists of the spatial/angular/epipolar plane image (EPI) feature extractor [33]. In the CVS-Net, 4 DD-Groups are cascaded

to accomplish multi-level spatial-angular feature separation and extraction. Then, we introduce the channel-wise attention module to achieve feature fusion. Finally, the angular down-sampling module is performed through channel descent to obtain the central SAI.

The CVS-Net is pre-trained by minimizing the absolute error between  $\tilde{I}_{u_0}$  and the central SAI  $I_{u_0}$ , which is expressed as follow:

$$\ell_{CVS} = \frac{1}{H \times W} \sum_{\mathbf{x}} |I_{u_0}(\mathbf{x}) - \tilde{I}_{u_0}(\mathbf{x})|. \quad (6)$$

## 4.2. Backward Degradation Network

As shown in Fig. 2(c), the BD-Net first converts the super-resolved LF images  $\hat{\mathcal{L}}^h$  into a degraded LR LF during forward propagation, then transmits the gradient from the loss function back to the HLFSSR-Net in backpropagation. Therefore, with the appropriate loss function, the BD-Net can guide the HLFSSR-Net to generate a reconstructed LF that accurately preserves the LF parallax structure corresponding to the input LF.

As shown in Fig. 2(b), the BD-Net is pre-trained using 2D HR images and the corresponding LF central SAIs. It is worth noting that the structure of the BD-Net varies depending on whether simulated or real hybrid data is being used.



For simulated data, the degradation process is relatively simple so we design the BD-Net based on VDSR [20], while the denoising network CBD-Net [12] is applied for the real-world data recorded by our hybrid system.

The BD-Net is pre-trained by minimizing the absolute error between  $\hat{I}_{u_0}$  and the central SAI  $I_{u_0}$ :

$$\ell_{BD} = \frac{1}{H \times W} \sum_{\mathbf{x}} |I_{u_0}(\mathbf{x}) - \hat{I}_{u_0}(\mathbf{x})|. \quad (7)$$

### 4.3. Hybrid LF Spatial SR Network

We design the HLFSSR-Net based on the characteristics of the hybrid input. As shown in Fig. 2(c), the HLFSSR-Net is divided into two branches, which perform feature extraction on the 2D HR image  $I_{u_0}^h$  (2D branch) and the 4D LR LF image  $\mathcal{L}$  (4D branch), respectively.

**Hybrid LF features extraction and fusion.** The spatial resolution of  $I_{u_0}^h$  is significantly higher than that of  $\mathcal{L}$ .  $I_{u_0}^h$  contains abundant high-frequency information missing from  $\mathcal{L}$ , which is essential for super-resolving the LR side-view SAIs without ground truth. As shown in Fig. 2(c), in the 2D branch, to fully extract the rich information of  $I_{u_0}^h$ , we utilize two Spatial-Conv modules to learn the initial features. Then we use a residual disentangling group (Distg-Group) [33] to further extract the high-frequency features, which are integrated by a Spatial-Conv module to obtain the HR features finally. In the 4D branch, 4 cascaded Distg-Groups are mainly used to extract the features of the LF structure. Following this, we up-sample these features to generate LF features that match the resolution of the HR LF  $\tilde{\mathcal{L}}^h$ . After extracting features in 2D and 4D branches, we combine them via concatenation. We utilize a Spatial-Conv module, a Distg-Group, and a Fusion-Conv module in sequence to learn the residual map. Finally, we add the residual map to up-sampled LF images  $\mathcal{L}$  by the bicubic interpolation to obtain the HR LF images  $\tilde{\mathcal{L}}^h$ .

**Loss function.** Based on the characteristics of the hybrid input, and to achieve unsupervised SR of side-view SAIs, we design the loss function with two parts.

For learning the detailed information from the 2D HR image  $I_{u_0}^h$ , the side-view SAIs in the super-resolved LF  $\tilde{\mathcal{L}}^h$  are reorganized and then fed into the CVS-Net to obtain the central SAI  $\hat{I}_{u_0}^h$ . We propose the HR-aware loss, which computes the absolute error between  $I_{u_0}^h$  and  $\hat{I}_{u_0}^h$ , as one of the loss function for training the HLFSSR-Net:

$$\ell_{hr} = \frac{1}{\alpha H \times \alpha W} \sum_{\mathbf{x}} |I_{u_0}^h(\mathbf{x}) - \hat{I}_{u_0}^h(\mathbf{x})|, \quad (8)$$

where  $\mathbf{x} = (x, y)$ ,  $1 \leq x \leq \alpha W$ ,  $1 \leq y \leq \alpha H$ .

To maintain the LF structure of the 4D LR LF image  $\mathcal{L}$ , the super-resolved LF  $\tilde{\mathcal{L}}^h$  is fed into the pre-trained BD-Net to obtain  $\tilde{\mathcal{L}}$  with the same resolution as the input LF  $\mathcal{L}$ . We

adopt the EPI gradient loss [15, 17] to enhance the parallax consistency between  $\tilde{\mathcal{L}}$  and  $\mathcal{L}$  to preserve the valuable LF parallax structure in the super-resolved LF  $\tilde{\mathcal{L}}^h$ . The EPI gradients are computed along both spatial and angular dimensions on both horizontal and vertical EPIs as follows,

$$\begin{aligned} \ell_{epi} = & \frac{1}{(N-1) \times \alpha H} \sum_{y,v} \left( \left| \nabla_x E_{y,v}(x, u) - \nabla_x \tilde{E}_{y,v}(x, u) \right| \right. \\ & \left. + \left| \nabla_u E_{y,v}(x, u) - \nabla_u \tilde{E}_{y,v}(x, u) \right| \right) \\ & + \frac{1}{(M-1) \times \alpha W} \sum_{x,u} \left( \left| \nabla_y E_{x,u}(y, v) - \nabla_y \tilde{E}_{x,u}(y, v) \right| \right. \\ & \left. + \left| \nabla_v E_{x,u}(y, v) - \nabla_v \tilde{E}_{x,u}(y, v) \right| \right), \end{aligned} \quad (9)$$

where  $\nabla$  is the differential operator,  $E_{y,v} = \mathcal{L}(x, y^*, u, v^*)$ ,  $E_{x,u} = \mathcal{L}(x^*, y, u^*, v)$ ,  $\tilde{E}_{y,v}$  and  $\tilde{E}_{x,u}$  denote the vertical and horizontal EPIs of the side-view SAIs  $\mathcal{L}_s$  and  $\tilde{\mathcal{L}}_s$ , respectively.

The aforementioned two loss functions, i.e. the HR-aware loss in Eq. (8) and the EPI gradient loss in Eq. (9), jointly constrain the learning of the HLFSSR-Net in the absence of the HR ground truth of the side-view SAIs. The end-to-end HLFSSR-Net is trained by minimizing the loss function:

$$\ell = \ell_{hr} + \ell_{epi} \quad (10)$$

## 5. Experiments

To evaluate our proposed unsupervised framework, we first train the HLFSSR-Net and compare it with SoTA methods on public LF datasets. Then, we perform an ablation study to validate and highlight the effectiveness of our proposed SR method. Finally, we apply the SR method to the hybrid LF dataset taken by our prototype.

### 5.1. Simulated Hybrid Datasets and Implementation Details

To the best of our knowledge, no public dataset is available for our HLFSSR-Net directly. We use 5 public LF datasets (HCI new [13], DLFD [27], EPFL [25], INRIA [22], STFgantry [29]) and follow [18] to generate simulated hybrid data by down-sampling off-center views of  $3 \times 3$  LF images and only retaining the resolution of the central views. We make the training and test datasets in HCI new and DLFD datasets following [18], and those in EPEL, INRIA and STFgantry datasets following [33].

In our training framework, we crop each SAI into patches of  $32 \times 32$  pixels, crop each corresponding 2D HR image into patches of  $64 \times 64$  pixels, and convert the RGB images to YCbCr color space for pre-training the CVS-Net and the BD-Net, and training the HLFSSR-Net. Specifically, according to [18, 33, 37], we only use the Y components for training and quantitative evaluation, while the Cb and Cr components are up-sampled by bicubic interpolation for the visual evaluation. We perform random horizontal

Table 1. Quantitative comparisons of different SR methods in terms of the number of parameters (#Param.) and PSNR/SSIM/LPIPS/EPIs’ SSIM for  $2\times$ SR on simulated hybrid data. Larger PSNR and SSIM values and smaller LPIPS values indicate higher SR quality. The best results for each of the NLB methods and ESLB methods are in **bold faces**. The difference between the results of our method and the best results are colored in **red** and **blue**, which represent the worse and the better results, respectively. The superscripts  $\dagger$  and  $\S$  represent different input modes: hybrid LF and LF only.

	Methods	#Param.	HCI new	DLFD	EPFL	INRIA	STFgantry	Average
NLB	Bicubic <sup>§</sup>	-	30.86/0.882/0.148/0.666	33.64/0.910/0.120/0.673	29.46/0.892/0.142/0.711	31.14/0.916/0.129/0.715	30.81/0.924/0.118/0.662	31.18/0.905/0.131/0.685
	PaSR <sup>†</sup> [5]	-	35.91/0.945/0.066/0.956	39.12/0.958/0.046/0.970	33.43/0.940/0.073/0.947	35.26/0.947/0.069/0.956	36.16/0.975/0.042/0.978	35.98/0.953/0.059/0.961
	iPADs <sup>†</sup> [31]	-	<b>37.98/0.965/0.008/0.969</b>	<b>40.42/0.972/0.006/0.978</b>	<b>35.54/0.961/0.010/0.964</b>	<b>36.13/0.951/0.014/0.958</b>	<b>38.53/0.983/0.006/0.985</b>	<b>37.72/0.966/0.009/0.971</b>
NLB v.s. Ours			-1.29/-0.020/+0.003/-0.014	-0.39/-0.015/+0.001/-0.008	-0.73/-0.022/+0.003/-0.017	-1.95/-0.034/+0.007/-0.026	-0.34/-0.009/+0.000/-0.004	-0.94/-0.020/+0.003/-0.014
ESLB	LFSSR <sup>§</sup> [37]	0.51M	37.36/0.978/0.018/0.976	39.41/0.983/0.017/0.984	34.03/0.971/0.035/0.966	36.05/0.982/0.027/0.978	37.42/0.988/0.012/0.987	36.85/0.980/0.022/0.978
	DistgSSR <sup>§</sup> [33]	2.65M	37.87/0.981/0.015/0.978	39.88/0.983/0.012/0.985	34.13/0.974/0.028/0.967	36.05/0.983/0.023/0.978	38.34/0.993/0.006/0.991	37.25/0.983/0.017/0.980
	EPIT <sup>§</sup> [24]	1.09M	38.01/0.980/0.021/0.978	40.22/0.984/0.018/0.985	34.17/0.973/0.028/0.967	36.10/0.983/0.024/0.979	<b>41.47/0.995/0.004/0.994</b>	37.99/0.983/0.019/0.981
	FHLFSR <sup>†</sup> [7]	0.53M	40.14/0.989/0.009/0.988	<b>44.06/0.994/0.004/0.994</b>	37.88/0.989/0.012/0.987	39.22/0.990/0.014/0.989	41.14/ <b>0.996/0.003/0.995</b>	40.49/ <b>0.992/0.008/0.991</b>
	LFHSR <sup>†</sup> [18]	9.90M	<b>41.27/0.990/0.008/0.989</b>	43.75/0.993/0.006/0.994	<b>39.21/0.991/0.007/0.989</b>	<b>40.99/0.991/0.010/0.990</b>	40.85/0.995/0.005/0.994	<b>41.21/0.992/0.007/0.991</b>
ESLB v.s. Ours			+2.00/+0.005/+0.003/+0.006	+3.25/+0.007/-0.001/+0.008	+2.94/+0.008/+0.000/+0.008	+2.91/+0.006/+0.003/+0.006	+2.60/+0.004/-0.003/+0.006	+2.55/+0.006/+0.001/+0.006
SSLB	LFZSSR <sup>§</sup> [10]	4.83M	32.48/0.949/0.077/0.948	35.34/0.965/0.052/0.967	31.97/0.959/0.053/0.952	33.85/0.973/0.039/0.969	32.81/0.966/0.041/0.965	33.29/0.962/0.054/0.960
USLB	Ours <sup>†</sup>	4.03M	39.27/0.985/0.005/0.983	40.81/0.987/0.005/0.986	36.27/0.983/0.007/0.981	38.08/0.985/0.007/0.984	38.87/0.992/0.006/0.989	38.66/0.986/0.006/0.985

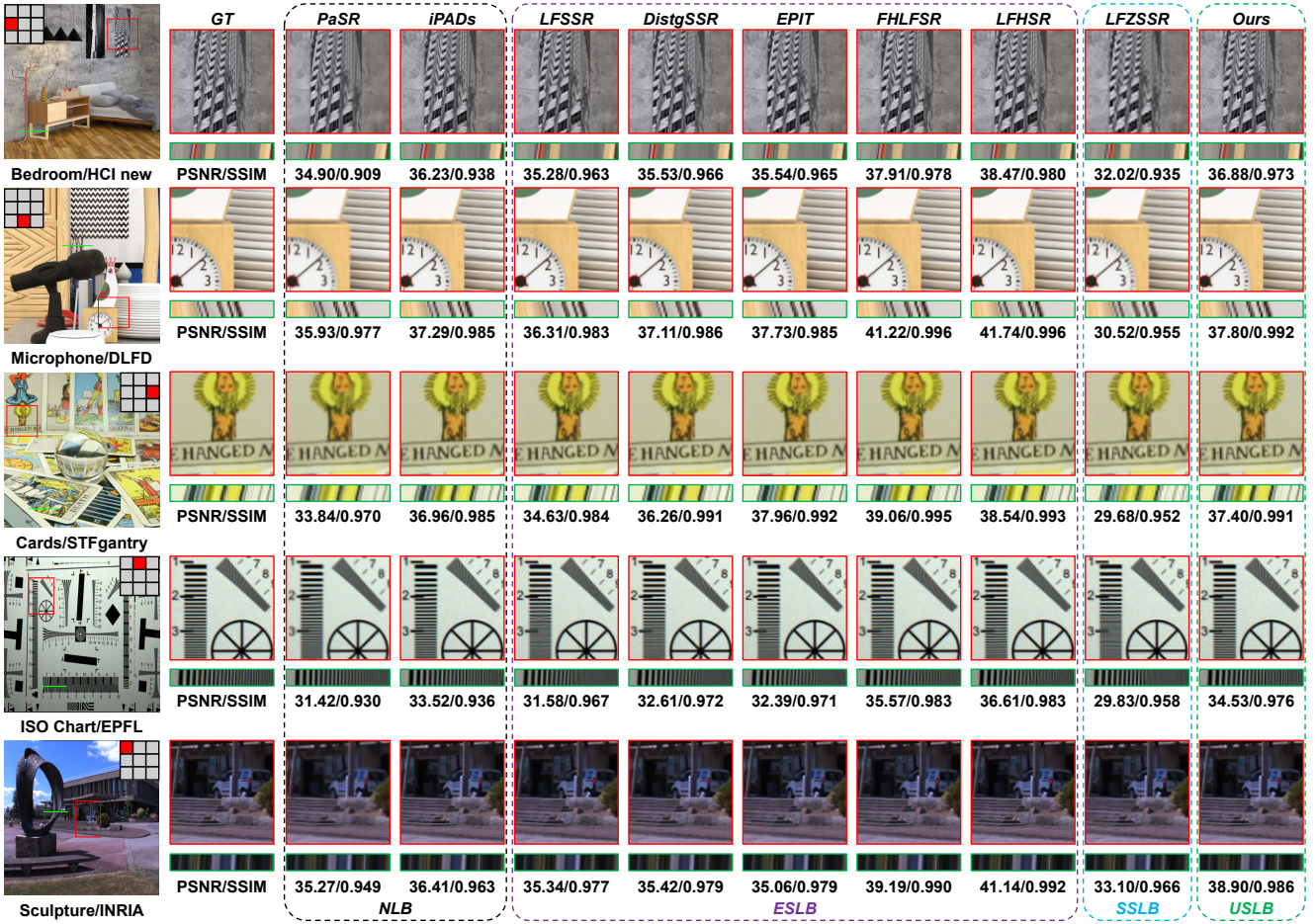


Figure 3. Visual comparisons for  $2\times$ SR on different simulated hybrid data. The PSNR and SSIM scores achieved by different methods on the presented scenes are reported below the zoom-in regions, and the horizontal EPIs are shown.

and vertical flipping, and 90-degree rotation in spatial and angular dimensions to augment the training data. We adapt Adam optimizer [21] with  $\beta_1 = 0.9$ ,  $\beta_2 = 0.999$  for both the pre-training and training stages. The learning rate is set to  $2 \times 10^{-4}$  initially and decreases by a factor of 0.5 every

15 epochs. Our networks are implemented in PyTorch on a PC with an NVIDIA RTX 3090 GPU.

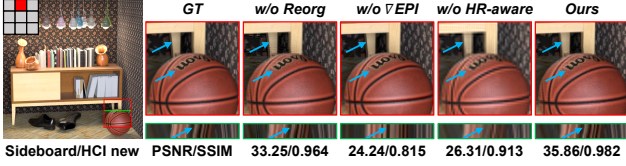


Figure 4. Visual illustration for ablation. The horizontal EPIs, PSNR and SSIM scores are illustrated below the zoom-in regions.

## 5.2. Comparisons with SoTA Methods

We compare our SR method with 8 SoTA methods, including 2 NLB methods (i.e., PaSR [5], iPADs [31]), 5 ESLB methods (i.e., LFSSR [37], DistgSSR [33], EPIT [24], FHLFSR [7], LFHSR [18]), and 1 SSLB method (i.e., LFZSSR [10]). Note that the 5 ESLB methods with training code released are retrained with the same training data for fair comparisons. The retrained models achieve comparable performance to those provided by the authors.

**Comparisons of quantitative results.** We compute PSNR, SSIM and LPIPS [41] in  $2\times SR$  side-view SAIs for quantitative comparisons. As listed in Tab. 1, compared to the NLB methods, our SR method produces the best performance with the best average PSNR, SSIM and LPIPS. When compared to the ESLB methods, our SR method outperforms 3 methods (i.e., LFSSR [37], DistgSSR [33] and EPIT [24]) that use only LF as input. However, it shows relatively weak performance compared to 2 methods (i.e., FHLFSR [7] and LFHSR [18]) that utilize hybrid input. According to the difference at the bottom of the ESLB in Tab. 1, although there is one-to-one ground truth for side-view SAIs of ESLB methods, our SR method still achieves acceptable performance.

**Comparisons of visual results.** We visually compare our  $2\times SR$  method with the 8 SoTA methods on the simulated hybrid datasets. As shown in Fig. 3, some close-up regions with abundant texture demonstrate that our SR method achieves similar performance in recovering the textures and details, especially compared with the ESLB methods such as FHLFSR [7] and LFHSR [18].

**Comparisons of LF parallax structure.** To evaluate the performance of maintaining the LF parallax structure, following [18, 37], we compare the EPIs. As depicted in Fig. 3, the EPIs obtained by our method show a clear linear texture as that of the ESLB methods. Furthermore, to provide a quantitative evaluation of the LF parallax structure, we compute the average SSIM of EPIs [18]. As listed in Tab. 1, our SR method achieves similar SSIM scores compared to the SoTA ESLB methods. Both the qualitative and quantitative results demonstrate that our SR method effectively preserves the LF parallax structure.

More comparisons and discussions are provided in the supplemental material.

Table 2. Ablation study for the proposed method. The quantitative results (PSNR/SSIM/LPIPS/EPIs’ SSIM) of  $2\times SR$  are provided.

$\nabla EPI$	HR-aware	LF-Reorg	HCI new	DLFD
✓	✓	-	36.41/0.969/0.017/0.967	38.32/0.976/0.013/0.979
-	✓	✓	27.37/0.884/0.021/0.894	29.25/0.908/0.021/0.920
✓	-	-	27.63/0.933/0.070/0.934	30.27/0.942/0.060/0.948
✓	✓	✓	<b>39.27/0.985/0.005/0.983</b>	<b>40.81/0.987/0.005/0.986</b>

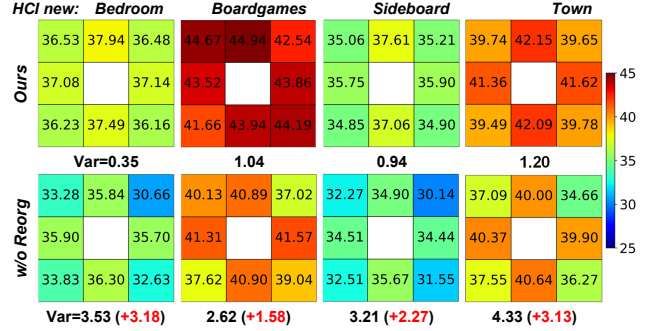


Figure 5. PSNR distribution among different side-view SAIs obtained by the frameworks with or without the LF reorganization. The variances (Var) in PSNR are listed below the heatmap.

## 5.3. Ablation study

We selectively remove the LF reorganization module, the EPI gradient loss, and the HR-aware loss from the complete framework to verify their effectiveness. As shown in Fig. 5, when we remove the LF reorganization module, not only the PSNR scores decrease, but also the variance of PSNR increases significantly. The ablation results demonstrate that the LF reorganization module ensures similar distributions of the side-view SAIs during backpropagation. As depicted in Tab. 2, when we eliminate the EPI gradient loss from the full framework, the PSNR scores on both datasets decrease over 10dB. In addition, the EPI shown in Fig. 4 illustrates that the HLFSSR-Net fails to maintain the LF parallax structure without the EPI gradient loss. Finally, as shown in Tab. 2, the SR performance also decreases when we remove the HR-aware loss, which is used to enhance the HLFSSR-Net’s ability to detail recovery. It should be noted that we remove the LF reorganization module after the HR-aware loss because the output of the CVS-Net, which includes the LF reorganization module, is used to compute the HR-aware loss. In summary, the results of the ablation study illustrate the indispensable importance of the two loss functions and the LF reorganization module.

## 5.4. Evaluation on Real-world Hybrid Dataset

To demonstrate the advantage of our unsupervised method, we conduct further evaluations on our real-world hybrid dataset described in Sec. 3. We apply the same pre-processing operations to the images in our hybrid dataset, as depicted in Sec. 5.1. As the ground truth HR LF images



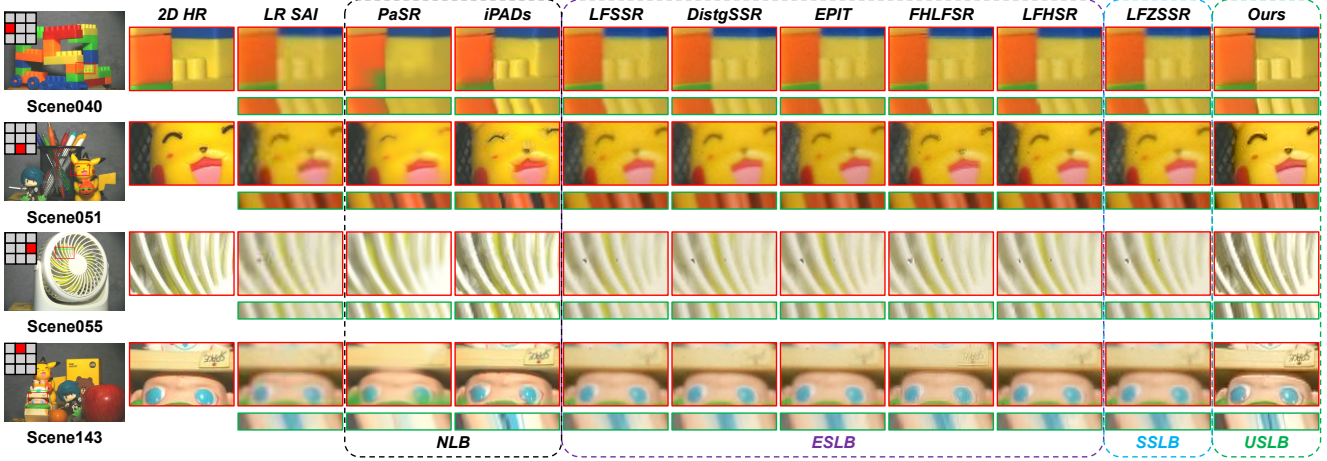


Figure 6. Comparisons of visual results and the LF parallax structure with different SR methods for  $2\times$ SR on our hybrid data. For each algorithm, we provide the zoom-in images of the red block and the horizontal EPIs.

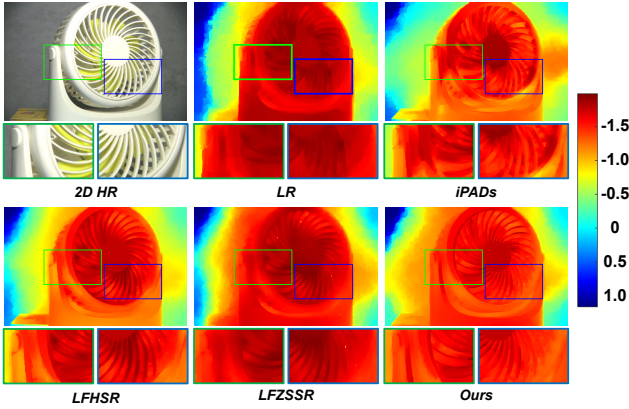


Figure 7. Visual comparisons of the estimated disparity maps from the LR LF images and super-resolved LF images by different methods on our real-world hybrid data.

are not available for supervision in our real hybrid dataset, we follow [18] to simulate hybrid datasets for training the ESLB networks [18, 24, 33, 37] to ensure fair comparisons. In addition, the NLB [5, 31] and SSLB [10] methods are performed on our real-world hybrid dataset directly.

Fig. 6 presents the visual comparisons of  $2\times$ SR results by different methods on our real-world hybrid dataset. It is evident that the SR results obtained by our hybrid network achieve the best visual performance. All of the NLB, SSLB and ESLB methods suffer from serious blur, such as the close-up building block, the shell of the fan and the faces of the toys. Although FHLFSR [7] and LFHSR [18] achieve better performance than our SR method in terms of PSNR and SSIM, all of the ESLB methods including FHLFSR [7] and LFHSR [18] suffer more serious blur than our SR method. This discrepancy could be attributed to the

difference between the degradation models learned from the simulated dataset and those learned from our real-world hybrid dataset. To demonstrate the performance of maintaining the LF parallax structure of our SR method, we compare the horizontal EPIs by different methods, as shown in Fig. 6. We also visually compare the disparity maps, as illustrated in Fig. 7, which are estimated from the LR LF images and the super-resolved LF images by different methods [10, 18, 31] using an identical LF disparity estimation algorithm [8]. The apparent linear structure of EPIs in Fig. 6 and the better disparity maps in Fig. 7 further illustrate the ability of our SR method to improve spatial resolution while preserving the inherent LF structure simultaneously.

## 6. Conclusion

To tackle the challenge of reconstructing HR LF images without ground truth, we first design a beam splitter-based hybrid LF imaging prototype and make a hybrid dataset. Moreover, we propose an unsupervised learning-based method for LF spatial SR, which adaptively settles the LF spatial SR problem with a complex degradation model. Specifically, we design two loss functions based on pre-training models, which enable the network to simultaneously learn the detail features and LF parallax structure without the ground truth of side-view SAIs. Extensive experiments demonstrate the considerable superiority of our approach compared with those external-supervised learning-based SoTA ones. To the best of our knowledge, this is the first end-to-end unsupervised learning-based method in the field of LF spatial SR. We believe our hybrid imaging prototype and unsupervised learning-based method could potentially promote LF SR methods to land on the ground.



## References

- [1] Lytro illum. <https://www.lytro.com/>. [Online]. 1
- [2] Raytrix. <https://www.raytrix.de/>. [Online]. 1
- [3] M Zeshan Alam and Bahadır K Gunturk. Hybrid light field imaging for improved spatial resolution and depth range. *Machine Vision and Applications*, 29(1):11–22, 2018. 2
- [4] Maliha Ashraf and Luis Ricardo Sapaico. Evaluation of color correction methods for printed surfaces. In *2018 Colour and Visual Computing Symposium (CVCS)*, pages 1–6, 2018. 3
- [5] Vivek Boominathan, Kaushik Mitra, and Ashok Veeraraghavan. Improving resolution and depth-of-field of light field cameras using a hybrid imaging system. In *2014 IEEE International Conference on Computational Photography (ICCP)*, pages 1–10, 2014. 1, 2, 3, 6, 7, 8
- [6] Zewei Cai, Xiaoli Liu, Xiang Peng, and Bruce Z Gao. Ray calibration and phase mapping for structured-light-field 3d reconstruction. *Optics Express*, 26(6):7598–7613, 2018. 1
- [7] Song Chang, Youfang Lin, and Shuo Zhang. Flexible hybrid lenses light field super-resolution using layered refinement. In *Proceedings of the 30th ACM International Conference on Multimedia*, page 5584–5592, New York, NY, USA, 2022. Association for Computing Machinery. 1, 2, 3, 6, 7, 8
- [8] Jie Chen, Junhui Hou, Yun Ni, and Lap-Pui Chau. Accurate light field depth estimation with superpixel regularization over partially occluded regions. *IEEE Transactions on Image Processing*, 27(10):4889–4900, 2018. 8
- [9] Yeyao Chen, Gangyi Jiang, Mei Yu, Haiyong Xu, and Yo-Sung Ho. Deep light field spatial super-resolution using heterogeneous imaging. *IEEE Transactions on Visualization and Computer Graphics*, 29(10):4183–4197, 2023. 1, 2, 3
- [10] Zhen Cheng, Zhiwei Xiong, Chang Chen, Dong Liu, and Zheng-Jun Zha. Light field super-resolution with zero-shot learning. In *Proceedings of the IEEE/CVF Conference on Computer Vision and Pattern Recognition (CVPR)*, pages 10010–10019, 2021. 1, 2, 6, 7, 8
- [11] Juliet Fiss, Brian Curless, and Richard Szeliski. Refocusing plenoptic images using depth-adaptive splatting. In *IEEE International Conference on Computational Photography (ICCP)*, pages 1–9, 2014. 1
- [12] Shi Guo, Zifei Yan, Kai Zhang, Wangmeng Zuo, and Lei Zhang. Toward convolutional blind denoising of real photographs. In *Proceedings of the IEEE/CVF Conference on Computer Vision and Pattern Recognition (CVPR)*, 2019. 5
- [13] Katrin Honauer, Ole Johannsen, Daniel Kondermann, and Bastian Goldluecke. A dataset and evaluation methodology for depth estimation on 4d light fields. In *Asian Conference on Computer Vision (ACCV)*, pages 19–34, 2017. 5
- [14] Berthold K.P Horn. Exact reproduction of colored images. *Computer Vision, Graphics, and Image Processing*, 26(2):135–167, 1984. 3
- [15] Jing Jin, Junhui Hou, Jie Chen, and Sam Kwong. Light field spatial super-resolution via deep combinatorial geometry embedding and structural consistency regularization. In *Proceedings of the IEEE/CVF Conference on Computer Vision and Pattern Recognition (CVPR)*, 2020. 1, 2, 5
- [16] Jing Jin, Junhui Hou, Jie Chen, Sam Kwong, and Jingyi Yu. Light field super-resolution via attention-guided fusion of hybrid lenses. In *Proceedings of the 28th ACM International Conference on Multimedia*, page 193–201, New York, NY, USA, 2020. Association for Computing Machinery. 1, 2, 3
- [17] Jing Jin, Junhui Hou, Hui Yuan, and Sam Kwong. Learning light field angular super-resolution via a geometry-aware network. In *Proceedings of the AAAI conference on artificial intelligence*, pages 11141–11148, 2020. 5
- [18] Jing Jin, Mantang Guo, Junhui Hou, Hui Liu, and Hongkai Xiong. Light field reconstruction via deep adaptive fusion of hybrid lenses. *IEEE Transactions on Pattern Analysis and Machine Intelligence*, 2023. 1, 2, 3, 5, 6, 7, 8
- [19] Changil Kim, Henning Zimmer, Yael Pritch, Alexander Sorkine-Hornung, and Markus H Gross. Scene reconstruction from high spatio-angular resolution light fields. *ACM Transactions on Graphics*, 32(4):73–1, 2013. 1
- [20] Jiwon Kim, Jung Kwon Lee, and Kyoung Mu Lee. Accurate image super-resolution using very deep convolutional networks. In *Proceedings of the IEEE conference on computer vision and pattern recognition*, pages 1646–1654, 2016. 5
- [21] Diederik P Kingma and Jimmy Ba. Adam: A method for stochastic optimization. *arXiv preprint arXiv:1412.6980*, 2014. 6
- [22] Mikael Le Pendu, Xiaoran Jiang, and Christine Guillemot. Light field inpainting propagation via low rank matrix completion. *IEEE Transactions on Image Processing*, 27(4):1981–1993, 2018. 5
- [23] Zhengyu Liang, Yingqian Wang, Longguang Wang, Jungang Yang, and Shilin Zhou. Light field image super-resolution with transformers. *IEEE Signal Processing Letters*, 29:563–567, 2022. 1, 2
- [24] Zhengyu Liang, Yingqian Wang, Longguang Wang, Jungang Yang, Shilin Zhou, and Yulan Guo. Learning non-local spatial-angular correlation for light field image super-resolution. In *Proceedings of the IEEE/CVF International Conference on Computer Vision (ICCV)*, pages 12376–12386, 2023. 1, 2, 6, 7, 8
- [25] Martin Rerabek and Touradj Ebrahimi. New light field image dataset. In *8th International Conference on Quality of Multimedia Experience (QoMEX)*, number CONF, 2016. 5
- [26] Hao Sheng, Sizhe Wang, Da Yang, Ruixuan Cong, Zhenglong Cui, and Rongshan Chen. Cross-view recurrence-based self-supervised super-resolution of light field. *IEEE Transactions on Circuits and Systems for Video Technology*, pages 1–1, 2023. 1, 2
- [27] Jinglei Shi, Xiaoran Jiang, and Christine Guillemot. A framework for learning depth from a flexible subset of dense and sparse light field views. *IEEE Transactions on Image Processing*, 28(12):5867–5880, 2019. 5
- [28] Langqing Shi and Ping Zhou. Learning based deep disentangling light field reconstruction and disparity estimation application. *arXiv preprint arXiv:2311.08129*, 2023. 4
- [29] Vaibhav Vaish and Andrew Adams. The (new) stanford light field archive. <http://lightfield.stanford.edu/lfs.html>. [Online]. 5
- [30] Ting-Chun Wang, Jun-Yan Zhu, Nima Khademi Kalantari, Alexei A. Efros, and Ravi Ramamoorthi. Light field video capture using a learning-based hybrid imaging system. *ACM Trans. Graph.*, 36(4), 2017. 2

- [31] Yuwang Wang, Yebin Liu, Wolfgang Heidrich, and Qionghai Dai. The light field attachment: Turning a dslr into a light field camera using a low budget camera ring. *IEEE transactions on visualization and computer graphics*, 23(10):2357–2364, 2016. 1, 2, 3, 6, 7, 8
- [32] Yunlong Wang, Fei Liu, Kunbo Zhang, Guangqi Hou, Zhenan Sun, and Tieniu Tan. Lfnet: A novel bidirectional recurrent convolutional neural network for light-field image super-resolution. *IEEE Transactions on Image Processing*, 27(9):4274–4286, 2018. 1, 2
- [33] Yingqian Wang, Longguang Wang, Gaochang Wu, Jungang Yang, Wei An, Jingyi Yu, and Yulan Guo. Disentangling light fields for super-resolution and disparity estimation. *IEEE Transactions on Pattern Analysis and Machine Intelligence*, 45(1):425–443, 2022. 1, 2, 4, 5, 6, 7, 8
- [34] Yang Yang, Lianxiong Wu, Lanling Zeng, Tao Yan, and Yongzhao Zhan. Joint upsampling for refocusing light fields derived with hybrid lenses. *IEEE Transactions on Instrumentation and Measurement*, 72:1–12, 2023. 1
- [35] Manhong Yao, Zixin Cai, Xue Qiu, Shiping Li, Junzheng Peng, and Jingang Zhong. Full-color light-field microscopy via single-pixel imaging. *Optics Express*, 28(5):6521–6536, 2020. 1
- [36] Wuyang Ye, Tao Yan, Jiahui Gao, and Yang Yang. Lfienet: Light field image enhancement network by fusing exposures of lf-dslr image pairs. *IEEE Transactions on Computational Imaging*, 9:620–635, 2023. 2
- [37] Henry Wing Fung Yeung, Junhui Hou, Xiaoming Chen, Jie Chen, Zhibo Chen, and Yuk Ying Chung. Light field spatial super-resolution using deep efficient spatial-angular separable convolution. *IEEE Transactions on Image Processing*, 28(5):2319–2330, 2018. 1, 2, 5, 6, 7, 8
- [38] Youngjin Yoon, Hae-Gon Jeon, Donggeun Yoo, Joon-Young Lee, and In So Kweon. Learning a deep convolutional network for light-field image super-resolution. In *Proceedings of the IEEE International Conference on Computer Vision (ICCV) Workshops*, 2015. 1, 2
- [39] Jingyi Yu. A light-field journey to virtual reality. *IEEE MultiMedia*, 24(2):104–112, 2017. 1
- [40] Yan Yuan, Ziqi Cao, and Lijuan Su. Light-field image super-resolution using a combined deep cnn based on epi. *IEEE Signal Processing Letters*, 25(9):1359–1363, 2018. 1, 2
- [41] Richard Zhang, Phillip Isola, Alexei A. Efros, Eli Shechtman, and Oliver Wang. The unreasonable effectiveness of deep features as a perceptual metric. In *Proceedings of the IEEE Conference on Computer Vision and Pattern Recognition (CVPR)*, 2018. 7
- [42] Shuo Zhang, Youfang Lin, and Hao Sheng. Residual networks for light field image super-resolution. In *Proceedings of the IEEE/CVF Conference on Computer Vision and Pattern Recognition (CVPR)*, 2019. 1, 2
- [43] Mandan Zhao, Gaochang Wu, Yipeng Li, Xiangyang Hao, Lu Fang, and Yebin Liu. Cross-scale reference-based light field super-resolution. *IEEE Transactions on Computational Imaging*, 4(3):406–418, 2018. 2
- [44] Haitian Zheng, Minghao Guo, Haoqian Wang, Yebin Liu, and Lu Fang. Combining exemplar-based approach and learning-based approach for light field super-resolution using a hybrid imaging system. In *Proceedings of the IEEE International Conference on Computer Vision (ICCV) Workshops*, 2017. 2, 3
- [45] Ping Zhou, Yanzheng Wang, Yuda Xu, Zewei Cai, and Chao Zuo. Phase-unwrapping-free 3d reconstruction in structured light field system based on varied auxiliary point. *Optics Express*, 30(17):29957–29968, 2022. 1